An Artificial Neural Network to Estimate the Foliar and Ground Cover Input Variables of the Rangeland Hydrology and Erosion Model

Mahmoud Saeedimoghaddam[a,*], Grey Nearing[b], David C. Goodrich[c], Mariano Hernandez[c], David Phillip Guertin[d], Loretta J. Metz[e], Haiyan Wei[d], Guillermo Ponce-Campos[d], Shea Burns[c], Sarah E. McCord[f], Mark A. Nearing[c], C. Jason Williams[c], Carrie-Ann Houdeshell[g], Mashrekur Rahman[a], Menberu B. Meles[h], Steve Barker[c]

[a]*Department of Land, Air & Water Resources, University of California, Davis, CA, USA*
[b]*Google Research, Mountain View, CA, USA*
[c]*USDA-Agricultural Research Service, Southwest Watershed Research Center, Tucson, AZ, USA*
[d]*School of Natural Resources and the Environment, University of Arizona, Tucson, AZ, USA*
[e]*USDA-NRCS Resource Inventory and Assessment Division, CEAP-Grazing Lands, Tucson, AZ, USA*
[f]*Jornada Experimental Range, US Department of Agriculture-Agricultural Research Service, Las Cruces, NM, USA*
[g]*USDA-NRCS Resource Inventory and Assessment Division, CEAP-Grazing Lands, Davis, CA, USA*
[h]*Sustainable Agricultural Water Systems Unit USDA-ARS, Davis, CA, USA*

Abstract

Models like the Rangeland Hydrology and Erosion Model (RHEM) are useful for estimating soil erosion, however, they rely on input parameters that are sometimes difficult or expensive to measure. Specifically, RHEM requires information about foliar and ground cover fractions that generally must be measured in situ, which makes it difficult to use models like RHEM to produce erosion or soil risk maps for areas exceeding the size of a hillslope such as a large watershed. We previously developed a deep learning emulator of RHEM that has low computational expense and can, in principle, be run over large areas (e.g., over the continental US). In this paper, we develop

*Corresponding author: Mahmoud Saeedimoghaddam, msaeedi@ucdavis.edu

a deep learning model to estimate the RHEM ground cover inputs from remote sensing time series, reducing the need for extensive field surveys to produce erosion maps. We achieve a prediction accuracy on hillslope runoff of $R^2 \approx 0.9$, and on soil loss and sediment yield of $R^2 \approx 0.4$ at 66,643 field locations within the US. We demonstrate how this approach can be used for mapping by developing runoff, soil loss, and sediment yield maps over a 1356 km2 region of interest in Nebraska.

Keywords: Deep Learning, Remote Sensing, Runoff, Soil Loss, Sediment Yield

1. Introduction

Deterioration of the U.S. rangelands is becoming an increasingly pressing and complex environmental issue (Geerken and Ilaiwi, 2004; Bedunah and Angerer, 2012; Gedefaw et al., 2021). Plant community transitions that degrade vegetation and ground cover on rangelands commonly increase runoff volume and soil erosion (Pierson et al., 2011; Turnbull et al., 2012; Williams et al., 2014). Loss of topsoil reduces rangeland health and productivity and typically removes organic and inorganic carbon from soil profiles (Schlesinger et al., 1996, 1999; Turnbull et al., 2010; Hernandez et al., 2017).

Models that estimate or predict erosion are critical tools for rangeland management - used in applications such as estimating soil vulnerability and assessing the impacts of soil protection policies (Flanagan et al., 2001). The Rangeland Hydrology and Erosion Model (RHEM) is a process-based hydraulic soil erosion prediction tool specific for rangeland applications that estimates runoff, soil loss, and sediment yield from storm events with sufficient accuracy (RHEM performance has been evaluated by the percent bias (PBIAS) (Gupta et al., 1999) and Root mean squared error-observations standard deviation ratio (RSR) (N. Moriasi et al., 2007)) for a wide range of applications (Nearing et al., 2011; Hernandez et al., 2017; Williams et al., 2022). A RHEM scenario includes four groups of input data (Al-Hamdan et al., 2015): 1- Climate station information, often from the CLImate GENerator (CLIGEN) model (Nicks et al., 1995), 2- Soil features, 3- Slope percentage and shape, and 4- Foliar cover fractions (Annual Forbs, Bunch Grass, Shrubs, Sod Grass) and Ground cover fractions (Litter, Biological Crusts, Basal, Rock).

Multiple sources of plot-scale surveyed data such as the US. Department

of Agriculture (USDA), Natural Resources Conservation Service(NRCS) Rangeland National Resource Inventory (NRI) have been used to create real-world RHEM scenarios (Weltz et al., 2014). Running RHEM at a plot scale (tens of square meters) provides insight into hydrologic and erosion patterns (Hernandez et al., 2013; Williams et al., 2022). Currently, running RHEM is mostly done at plot scales. However, because the fourth category of input variables (foliar and ground cover) requires expensive, local field surveys, applying RHEM to larger areas or regions in a spatially explicit manner (e.g. to create soil vulnerability maps) is currently difficult (McGwire et al., 2020). Similarly, it is not possible to survey the past, meaning that running counterfactual experiments with RHEM, for example, to assess the impacts of specific rangeland management strategies, is also difficult or challenging. Thus, we need an alternative way to parameterize (provide input data to) RHEM that can be applied in areas that have not been surveyed (which comprises the majority of land in the continental US) and that uses data that are available in the past (strategies like the extrapolation of the existing surveyed data can introduce modeling uncertainty because of the coarse temporal and spatial resolution of such data).

Aside from foliar (Annual Forbs, Bunch Grass, Shrubs, Sod Grass) and ground (Litter, Biological Crusts, Basal, and Rock) cover variables, the other inputs to RHEM are available from mapped, gridded datasets. Soil texture are available from multiple sources such as the SoilGrids dataset (Hengl et al., 2017) or Gridded Soil Survey Geographic dataset (USDA, 2020). Topography (Elevation) information is available globally at 30 meters, from sources like Copernicus Digital Elevation Model (GLO-30) (Airbus, 2022). However, there is no nationwide data source for the foliar and ground cover fractions that provide the categories required by RHEM. To the best of our knowledge, there are two available nationwide time series datasets of rangeland fractional cover in the US.:

- The Rangeland Analysis Platform created by Allred et al. (2021) by building on Jones et al. (2018) can be accessed from `rangelands.app`. This data set estimates Annual Forb and grass, Perennial forb and grass, Shrubs, tree, Litter, and bare ground fractional covers for the United States at 30-meter resolution back to 1986 with a reported mean absolute error (MAE) of 6.3%. This product was developed by training a multi-output artificial neural network (ANN) to estimate cover variables from time series of Landsat images.

- The vegetation cover product of the Landscape Fire and Resource Management Planning (LANDFIRE) project created by the US. Department of Agriculture Forest Service and the US. Department of the Interior (Nelson et al., 2016), accessed from `landfire.gov`. This nationwide data contains tree, Shrubs, and herb covers percentages in 30 meters resolution (available for 2001, 2012, 2014, 2016, and 2020). Several field-based and remote sensing data sources have been utilized for creating the LANDFIRE data set (Rollins, 2009).

The fractional cover categories of the above datasets are not fully compatible with the RHEM's cover inputs. In addition, the indicators used to assess the overlapping categories may not be necessarily aligned. For instance, RHEM relies on the "Surface Litter" indicator whereas other datasets or applications may focus on Litter anywhere in the canopy (e.g., any hit) or only at the top of the canopy or in the interspaces (first hit). Surface Litter is the cover of total Litter, both detached herbaceous Litter, detached woody Litter, duff, and non-vegetative Litter where Litter is directly covering the soil surface in the plot, not including Litter that has plant, or biological crust below it. Litter over rock is considered Litter (For example, points with sagebrush over Litter over soil are counted in this indicator, while Litter over sagebrush over soil is not counted). Artificial Litter and non-vegetation Litter are excluded from this indicator (Karl et al., 2017; McCord et al., 2022).

Some prior studies estimated the fractional covers for RHEM use. Kautz et al. (2019) estimated the total foliar cover of a region in southeastern Arizona using a linear regression between the Landsat data products and field survey data (the MAE and the R^2 of the best model are 4.6 and 0.85 respectively). They estimated Litter and Basal cover from the total foliar cover using two separate linear regressions fitted to field surveyed data. Also, for an area around the four-corners area (Utah, Colorado, New Mexico, and Arizona), McGwire et al. (2020) approximated total foliar cover using a linear relationship between Landsat and NRI data ($R^2 = 0.69$). They estimated Shrubs, Annual Forbs, and Bunch Grass from LANDFIRE data. They calculated the Litter cover and Basal cover from the total foliar cover using two separate linear regressions (R^2 of 0.709 and 0.13 respectively) fitted to the NRI data. Finally, the Rock cover was estimated by the method of Nauman et al. (2019). Both of these studies used remote sensing data exclusively for estimating total foliar cover, and not for estimating the detailed categories.

In addition, the detailed foliar cover categories were based on LANDFIRE data which is not available for every date of interest.

In this study, we present an ANN model that estimates the foliar/ground fractional covers in accordance with the RHEM requirements. By utilizing time series of Landsat images (available since 1982) and climatic features (available since 1895), as well as information about soil texture and latitude/longitude, our model estimates Annual Forbs, Bunch Grass, Shrubs, Sod Grass, Litter, Biological Crusts, Basal, and Rock fractions for any location and date. We trained the ANN using multiple plot scale (surveyed) datasets of the U.S. rangelands. Having the foliar/ground cover RHEM inputs from our model, we would be able to create the maps of the runoff, soil loss, and sediment yield for any location and date after Spring, 1987 (The first Landsat 4 TM images are from Summer 1982. Our model takes 5 years of images prior to the date of mapping as inputs (see section 2.1). Therefore, the first possible date to make the RHEM maps is in Summer, 1987). Previously, Woznicki et al. (2020) created the nationwide U.S. maps of the soil loss and sediment yield using the Revised Universal Soil Loss Equation (RUSLE). However, RUSLE empirical method does not properly return the hillslope-scale soil erosion process on rangelands (McGwire et al., 2020). So, McGwire et al. (2020) used RHEM to map the sediment yield risk of the saline rangelands of the Mancos Shale formation in Utah, Colorado, New Mexico, and Arizona. However, as was mentioned before, the foliar cover categories in this study were captured from LANDFIRE data, making it impossible to create the maps for every date of interest. Our approach directly estimates all of the foliar/ground cover inputs of the RHEM from the remote sensing data. Therefore, the temporal availability of the Landsat data is the only restriction for building RHEM maps.

2. Materials and methods

In this section, we start by introducing the architecture of the ANN that estimates the foliar and ground cover inputs of the RHEM by the remote sensing data. Then, we describe the rangeland field data plots and the remote sensing data sources that are used for training the ANN. Finally, we describe the sources of the other RHEM inputs and the emulator of the RHEM used for calculating and mapping the runoff, soil loss, and sediment yield for the selected region.

2.1. The architecture of the foliar/ground cover estimator

Figure 1 demonstrates the architecture of the ANN that estimates the foliar and ground cover for the RHEM. The model has multiple input channels. It starts with the first input channel which is the time series of the Landsat images with (20,3,3,22) dimensions. The 20 is the temporal dimension and is seasonal. For instance, if we are going to estimate the cover of a location for Summer 2020, the time series starts in Fall 2020 and ends in Summer 2020. The (3,3) are the spatial dimensions and the 22 is the number of features including 6 bands of the Landsat and 16 indices like NDVI, EVI, etc. (Table 1). This input channel is fed into two 2D Partial Convolution layers. Partial Convolution (Liu et al., 2018) is a version of the convolution layer that can mask the pixel with no data and ignore them in the calculations. This ability is very useful for handling the satellite image input channels in which some pixels (like the cloud-covered ones) are usually marked as no data. The function of these two Partial Convolution layers is to determine how the pixels within each plot sample will be aggregated. Previous studies had combined the pixels during the pre-processing stage (Allred et al., 2021), but our approach allows the neural network to determine the significance of each pixel in every 22 features and aggregate them spatially based on their importance. Both of the Partial Convolution layers of the model have 64 filters, (1,1) kernel size, valid padding, and stride of 1. Also, one of the layers has the Parametric Rectified Linear Unit activation function (PReLU) (He et al., 2015). (1,1) kernel size means that the layers do not change the spatial dimension of the data and it creates 64 features out of 22 features of the input data. The output of the Partial Convolution layer with no activation is fed into a Softmax function which operates over its spatial dimensions to calculate a weight between 0 and 1 for each pixel. The weights sum up to one for each and every 64 features. It should be noted that the pixels with no data values are ignored by the Softmax operator. The weights are then used to calculate the weighted average of the pixels of the output of the Partial Convolution with PReLU activation over its (3,3) spatial dimensions. The output of the weighted average is a 2D vector of 20 time steps and 64 features. The second input channel of the ANN is the time series of the PRISM climate dataset (see section 2.4.2) with (20,2) dimensions. The 20 is the temporal dimension and is seasonal. It also has 2 features which are precipitation and mean temperature. The PRISM input channel is concatenated with the output of the spatial average operator to make a (20,66) dimensional vector. The vector is then fed into a Recurrent Neural Network (RNN) layer with

128 units and the hyperbolic tangent activation function. The output of the RNN layer is a single vector of shape 128 containing information about the entire time series. The third input channel of the ANN model has 11 features including 1- The Latitude and Longitude of the location of the input, 2- The information about the soil of the location of the input such as porosity, mean capillary drive, etc. (Table 2). This channel is concatenated with the output of the RNN layer to make a vector of shape 139. This vector is then fed into a series of fully connected layers. The size of each layer is 256 and they all have PReLU activation functions. After each of these fully connected layers, there is a Dropout layer (Srivastava et al., 2014) that randomly deactivates 10% of the neurons to address any unintended overfitting of the model. The output of the last layer of this series is fed into a fully connected layer of size 128 and the PReLU activation function. Finally, the output of this layer is passed into two fully connected layers each of size 5 with the Softmax activation functions. One of these layers estimates the fractions of the four categories of ground cover at the input location: Litter, Biological Crusts, Basal, and Rock covers. Since the Softmax output sums up to 1, we include a fifth category: (1 - Total Ground Cover). Similarly, the other layer estimates the fractions of the four categories of foliar cover at the input location: Annual Forbs, Bunch Grass, Shrubs, Sod Grass along with (1 - Total Foliar Cover).

Overall, the ANN model has 233,484 trainable parameters. Through multiple objective-subjective trials, we decided on the number of layers, their sizes, and their activation functions.

2.2. Model Training

We trained the foliar/ground cover estimator for 24 epochs with an Adam optimizer (Kingma and Ba, 2014) and a batch size of 40. The learning rate of the optimizer is equal to 0.001 for the first 8 epochs (train over the entire training dataset 8 times). It decreases as follows: 5×10^{-4} for epochs 9 to 15, 1×10^{-4} for epochs 16 to 20, 5×10^{-5} for epochs 21 and 22, and 1×10^{-5} for epochs 23 and 24. The loss function is Mean Squared Error (MSE). The above settings have been chosen by the manual trials.

Finally, the model and all analyses were implemented in Python. The model was developed as a Keras module using Tensorflow2 (Abadi et al., 2015).

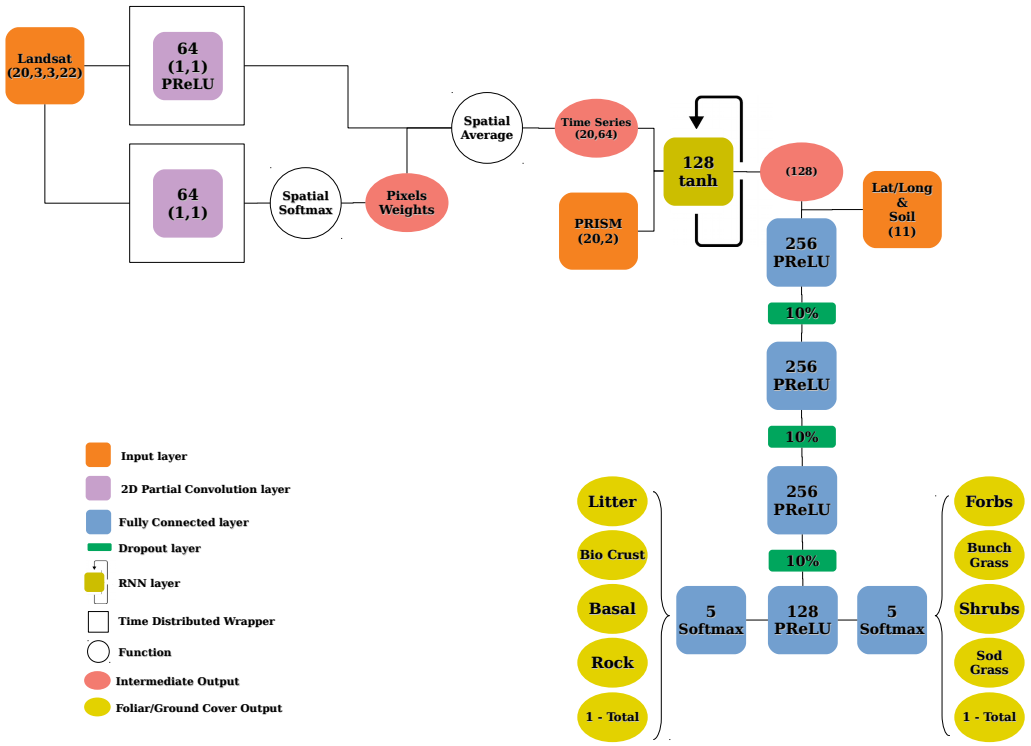

Figure 1: The architecture of the artificial neural network that estimates the foliar and ground cover inputs of the RHEM by the remote sensing data (RNN: Recurrent Neural Network, PReLU: Parametric Rectified Linear Unit, PRISM: Parameter-elevation Regressions on Independent Slopes Model).

2.3. Model accuracy analysis

We evaluate the performance of the foliar/ground cover estimator by comparing its outputs with the observed covers. In addition, we demonstrate the effectiveness of the model estimations in reproducing the actual RHEM outputs.

2.3.1. The accuracy of the foliar/ground cover estimator

In this study, we report three metrics suggested by Gupta et al. (2009) to assess the performance of the foliar/ground cover estimator:

1- Coefficient of determination (R^2):

$$R^2 = 1 - \frac{\frac{1}{N}\sum_{n=1}^{N}(o_n - e_n)^2}{\sigma_o^2} \tag{1}$$

where o is the observed value of the output, e is the model estimation of the output, N is the data size and, σ_o^2 is the variance of the observed values.

2- α-R^2 decomposition which measures the relative variability in the estimated and observed values:

$$\alpha = \frac{\sigma_s}{\sigma_o} \tag{2}$$

where σ_s is the standard deviation of the model estimation of the output and σ_o is the standard deviation of the observed output values.

3- β-R^2 decomposition which captures the normalized bias in the model estimation:

$$\beta = \frac{\mu_s - \mu_o}{\sigma_o} \tag{3}$$

where μ_s is the average of the model estimation values and μ_o is the average of the observed values.

We use these metrics across 10-fold cross-validation experiments (90% of the data or 59,979 samples for training and 10% or 6,664 samples for the test). We also investigate the effect of input data source alteration on the model performance by training the model using NRI data source and testing it by the Bureau of Land Management (BLM) (see section 2.4.1 for information about the data sources), and vice versa.

Since the previous study on rangeland cover estimation (see table 4) used root mean squared error (RMSE) and mean absolute error (MAE) as performance measures, we also use these in addition to normalized RMSE (nRMSE) and normalized MAE (nMAE) (RMSE and MAE divided by the average of the observed values) to facilitate comparison.

2.3.2. The accuracy of the RHEM outputs using the estimated covers

The primary goal of estimating the foliar/ground covers is to apply the RHEM to locations without any surveyed data. To assess the effectiveness of the estimated covers in reproducing the actual RHEM outputs, we run the RHEM using both observed and estimated covers and compare them using the R^2, α, β measures. Instead of executing the RHEM by its original software available on `dss.tucson.ars.ag.gov/rhem/`, to speed up the process, we use the RHEM neural network emulator (Saeedimoghaddam et al., 2022) using a single GPU which produces the RHEM outputs 13 billion times faster with high accuracy.

2.4. Data

2.4.1. The rangeland field data plots

We used two sets of field measurement data plots. First, the NRI dataset (Figure 2a shows its geographic distribution). Since 2004, the USDA NRCS has conducted the NRI on rangelands held in non-federal ownership (privately deeded, state-owned, tribal lands, and local government-owned lands) (Nusser and Goebel, 1997; USDA, 2018). The NRI plots are circular areas with a diameter of 45.7 m, covering 0.16 ha, centered on the NRI points. The two transects along the diameters are sampled using the line-point intercept methods (Herrick et al., 2018). The second set of field measurement data comes from the BLM (Figure 2b shows its geographic distribution). Since 2011, BLM monitors about 991,480 km2 of public lands within 12 western states using the Assessment, Inventory, and Monitoring (AIM) terrestrial data collection strategy. In the AIM strategy, the sampling is done using the line-point intercept methods as well (Toevs et al., 2011). The Landscape Monitoring Framework (LMF) is a part of the AIM strategy to oversee renewable resources on public rangelands (Kachergis et al., 2022). The AIM plot size is usually about 0.28 ha but it may vary in different projects, while the LMF plots are 0.16 ha. For more information about the AIM monitoring protocols, please refer to Herrick et al. (2018). NRI and LMF use a paired two-stage cluster sampling design (Yu et al., 2020) whereas AIM often uses a generalized random tessellation stratified sampling approach (Kachergis et al., 2022).

We prepared 66,643 field-measured foliar/ground cover data from 32,426 NRI plots and 34,217 AIM plots. Each plot contains information on the field's foliar/ground cover, the survey date-time, and a unique index. The percent cover for the Litter, Biological Crusts, and Rock categories was calculated by the any hit pin drop data, while for Basal cover, the Basal hit was utilized. Meanwhile, for Annual Forbs, Bunch Grass, Shrubs, and Sod Grass, first hit pin drop data was used to determine their percentage of coverage (McCord et al., 2022). Figure 3 compares the distributions of the calculated foliar and ground percent covers between NRI and BLM datasets. The two datasets exhibit similar distribution patterns for Annual Forbs cover, but there are notable differences in the distribution shapes for other categories such as Litter and Shrubs. The difference between the patterns of the two datasets could be the result of their geographical distributions, the time periods of measurements, and land ownership. The BLM plots are exclusively situated

in public lands in the western United States, whereas the NRI plots are dispersed across private lands throughout the country, primarily in the Great Plains states (Figure 2).

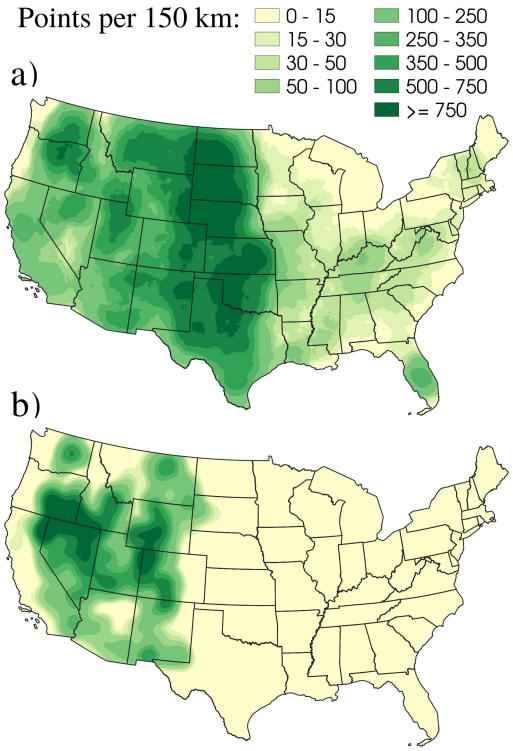

Figure 2: The density map of a) NRI and b) BLM data plots

2.4.2. The data sources of the model inputs

For each survey plot, we downloaded all the Landsat (Landsat 4 to 8) images (30 m resolution) of the last five years before the survey date from the Google Earth Engine (GEE) data catalog (Gorelick et al., 2017). We acquired the surface reflectance products in an area of 3 × 3 pixels around the center of the plot (smaller areas e.g. 2 × 2 pixels may not cover the entire plot, especially for the AIM data. Also, a bigger area e.g. 4 × 4 pixels may add irrelevant information to the model). We got bands 1,2,3,4,5,7 for Landsat 4 to 7 and bands 2,3,4,5,6,7 for Landsat 8. We also got the pixel quality band for detecting unwanted pixels. The following types of pixels were masked: 1- pixels with out-of-range values (less than 0 or greater than

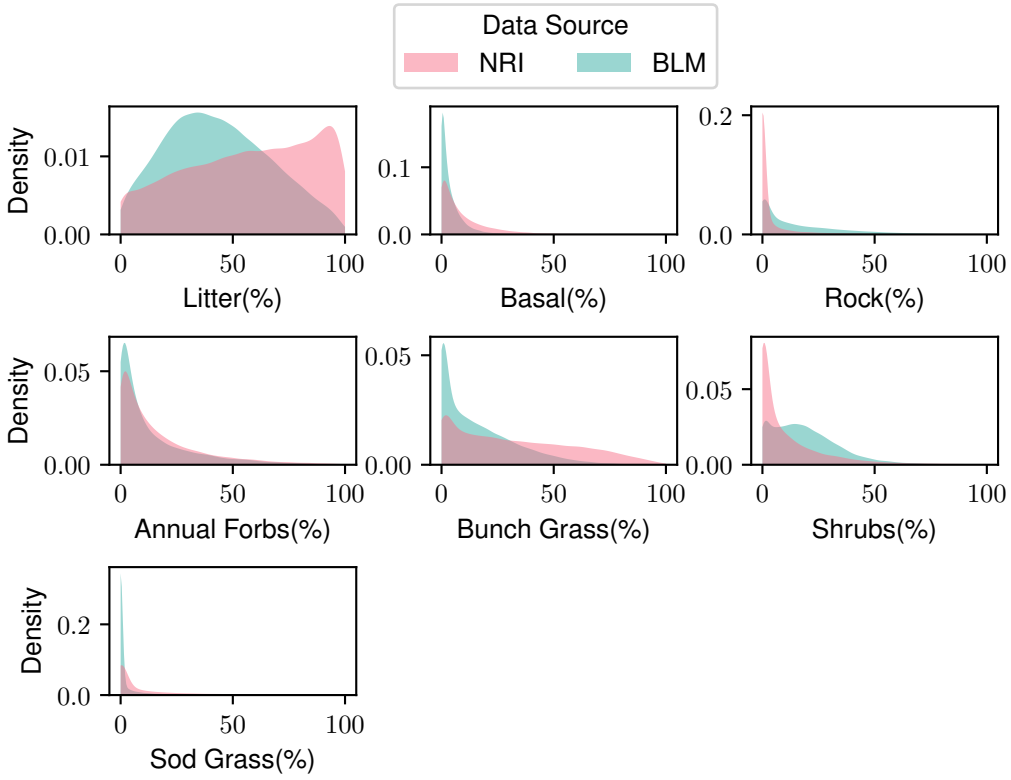

Figure 3: Comparing the distributions of the observed foliar and ground cover values between NRI and BLM datasets

1) such as saturated pixels, 2- pixels which are not flagged as clear according to the pixel quality band (the clear pixel codes are 66, 68, 72, 80, 96, 112 for Landsat 4 to 7 (Sayler and Zanter, 2020a) and are 322, 386, 834, 898, 1346 for Landsat 8 (Sayler and Zanter, 2020b)). Next, we harmonized the surface reflectance values of Landsat 8 with those from Landsat 4 to 7 as they have different wavelength ranges. For that, we used the equations from Table 2 of Roy et al. (2016). In addition, we added the 17 Landsat surface reflectance-derived spectral indices that help to detect the different foliar/ground cover categories. Table 1 shows the 6 Landsat bands as well as the indices that we used in this study. Finally, we converted the daily time series into a seasonal one. We calculated the average of the images per season and made a (20,3,3,22) vector for each plot (20 seasons in 5 years, 3×3 pixels, and, 22 channels).

Table 1: The Landsat bands and the extracted indices as the 22 features of the first model input

Band		
Blue, Green, Red, Near Infrared (NRI), Shortwave Infrared 1 (SWIR1), Shortwave Infrared 2 (SWIR2)		
Index	**Formula**	**Application in the Vegetation/Ground Cover Estimation[1]**
NDVI (normalized difference vegetation index)	$\frac{NIR-R}{NIR+R}$	Senseman et al. (1996); Karnieli (1997); Sivanpillai and Booth (2008); Chen and Gillieson (2009); Cao et al. (2010); Jansen et al. (2016, 2018); Jones et al. (2018); Naji (2018); Pei et al. (2018); Kautz et al. (2019); Abdolalizadeh et al. (2020); Allred et al. (2021)
EVI (enhanced vegetation index)	$2.5 \times \frac{NIR-R}{NIR+6\times Red-7.5\times Blue+1}$	
SAVI (soil adjusted vegetation index)	$1.5 \times \frac{NIR-R}{NIR+R+0.5}$	
MSAVI (modified soil adjusted vegetation index)	$\frac{2\times NIR+1-\sqrt{(2\times NIR+1)^2-8\times(NIR-Red)}}{2}$	
SATVI (soil adjusted total vegetation index)	$1.5 \times \frac{SWIR1-Red}{SWIR1+Red+0.5} - \frac{SWIR2}{2}$	
PVI (perpendicular vegetation index)[2]	$(\sin(\alpha) \times NIR) - (\cos(\alpha) \times Red)$	
KBRI (Karst bare Rock index)	$\frac{SWIR1-NIR}{20\times\sqrt{SWIR1+NIR}}$	
NDMI (normalized difference moisture index)	$\frac{NIR-SWIR1}{NIR+SWIR1}$	
NBR (normalized burn ratio)	$\frac{NIR-SWIR2}{NIR+SWIR2}$	
NBR2 (normalized burn ratio 2)	$\frac{SWIR1-SWIR2}{SWIR1+SWIR2}$	
TC_b (Tasseled-Cap Brightness)	$Blue \times 0.2043 + Green \times 0.4158 + Red \times 0.5524 + NIR \times 0.5741 + SWIR1 \times 0.3124 + SWIR2 \times 0.2303$	
TC_g (Tasseled-Cap Greenness)	$Blue \times -0.1603 + Green \times 0.2819 + Red \times -0.4934 + NIR \times 0.7940 + SWIR1 \times -0.0002 + SWIR2 \times -0.1446$	
TC_w (Tasseled-Cap Wetness)	$Blue \times 0.0315 + Green \times 0.2021 + Red \times 0.3102 + NIR \times 0.1594 + SWIR1 \times -0.6808 + SWIR2 \times -0.6109$	
CI (crust index)	$1 - \frac{Red-Blue}{Red+Blue}$	
DFI (dead fuel index)	$(1 - \frac{SWIR2}{SWIR1}) \times \frac{Red}{NIR}$	
NDSI (normalized difference snow index)	$\frac{Green-SWIR1}{Green+SWIR1}$	

[1] The studies on the Vegetation/Ground cover estimation in general not necessarily in rangelands.
[2] α is the angle between the soil line and the NIR axis in the Red-NIR scatterplot (Naji, 2018).
[3] The Tasseled Cap formulas are from Crist (1985), the KBRI formula is from Pei et al. (2018) and, the DFI formula is from Cao et al. (2010).

Table 2: The values of the soil parameters for each texture class.

Soil Texture Class	por	dist	G	smax	frac1	frac2	frac3	frac4	frac5
Sand	0.3902	0.69	50	0.95	0.0077	0.018	0.0435	0.148	0.7827
Loamy Sand	0.4087	0.55	70	0.92	0.0137	0.0353	0.0951	0.233	0.6229
Sandy Loam	0.4306	0.38	130	0.91	0.0325	0.0542	0.1801	0.3939	0.3394
Loam	0.4531	0.25	110	0.94	0.0498	0.1128	0.2877	0.4004	0.1494
Silt Loam	0.4455	0.23	200	0.97	0.0505	0.3095	0.3497	0.2255	0.047
Silt	0.4258	0.23	200	0.97	0.0221	0.682	0.153	0.0916	0.0513
Sandy Clay Loam	0.4377	0.32	260	0.83	0.0641	0.0005	0.1686	0.6217	0.1451
Clay Loam	0.4589	0.24	260	0.84	0.0848	0.0397	0.3157	0.5148	0.045
Silty Clay Loam	0.4581	0.18	350	0.92	0.0861	0.1986	0.4014	0.3044	0.0096
Sandy Clay	0.4146	0.22	305	0.75	0.1073	0.0001	0.1039	0.7544	0.0344
Silty Clay	0.4704	0.15	375	0.88	0.1196	0.1517	0.3244	0.4012	0.0031
Clay	0.4724	0.16	400	0.81	0.1247	0.0001	0.2567	0.6057	0.0128

* por: Porosity, dist: Pore size distribution, G: Mean capillary drive (mm), smax: Upper limit to saturation, frac1-5: Particle class fractions

For the second input channel of the model, we downloaded the monthly precipitation and mean temperature from the Parameter-elevation Regressions on Independent Slopes Model (PRISM) (Oregon State University, 2014) on the GEE repository. First, we Normalized the values by the (min, max) ranges which are (0, 731.663) millimeters for the precipitation and (-40.009, 49.048) $^{\circ}C$ for the mean temperature within the US. contiguous states according to the PRISM dataset. Then, we converted the monthly data to seasonal data by averaging it.

Finally, for the third input channel, we used the SoilGrids dataset (Hengl et al., 2017) to get the soil texture of each plot. The textures are based on the USDA soil classification Soil Survey Staff (1999). Pedotransfer functions have been used to estimate soil hydraulic properties. These are very important to estimate infiltration parameters (Zhang and Schaap, 2017). We have used nine hydrological and soil particle parameters for each texture. Table (2) lists the soil texture classes as well as their parameters.

2.5. Mapping the RHEM outputs

One major benefit of the foliar/ground cover estimator is that it allows us to extrapolate the RHEM outputs to the locations where foliar/ground cover information is unknown. This means we can map the RHEM outputs for any region in the contiguous US and for all seasons after Summer, 1987. To demonstrate this, we mapped the RHEM outputs for Keith County, Nebraska during Summer 2020, which lies within Major Land Resource Area (MLRA) 65 (USDA, 2022) (Figure 4a). The spatial resolution of the map is 90 meters (three times the Landsat data resolution) since the foliar/ground cover estimator expects a 3×3 spatial dimension for the input. We selected

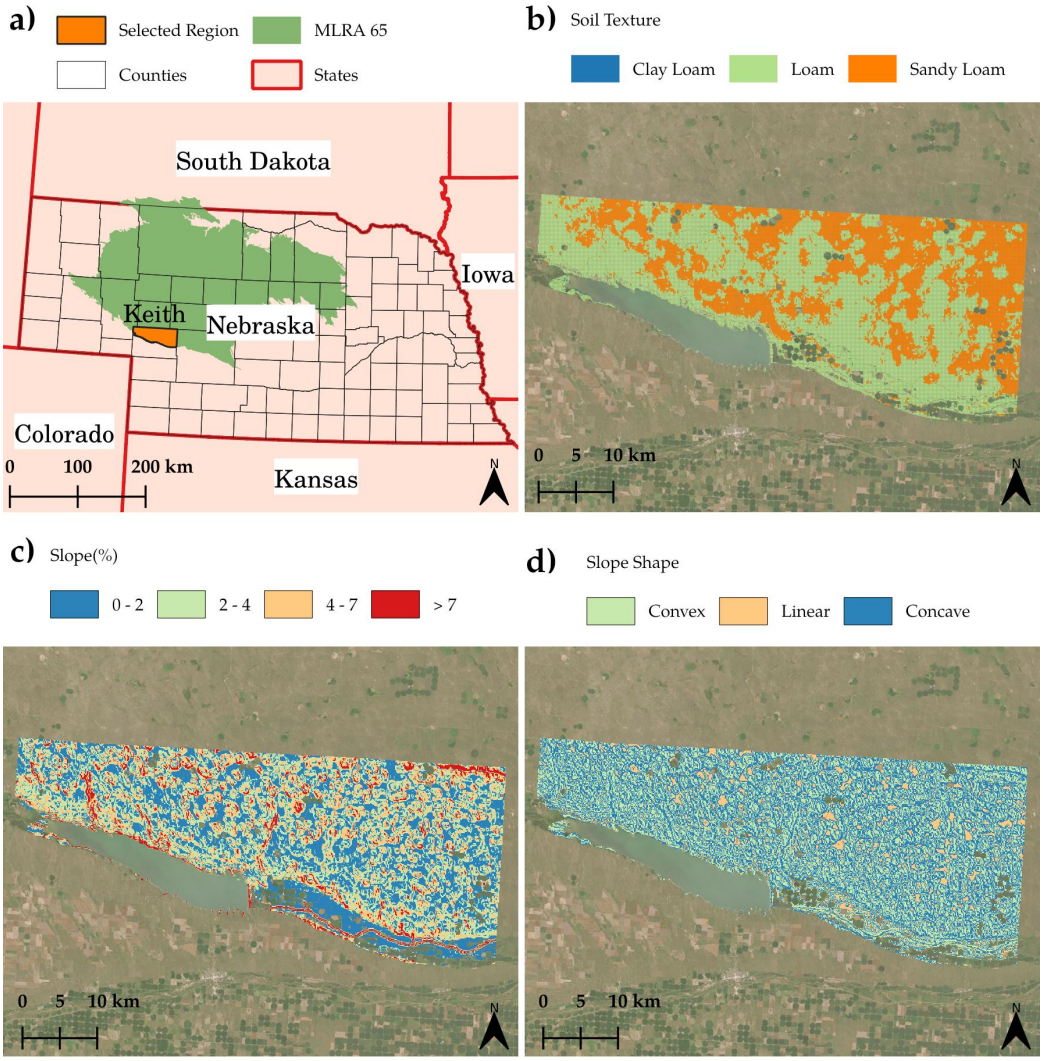

Figure 4: a) The selected region for mapping the RHEM outputs, b) The soil texture map of the region, c) The slope map of the region, d) The slope shape map of the region.

*MLRA: Major Land Resource Area (USDA, 2022)

the National Land Cover Database (NLCD) 2019 (Wickham et al., 2021) as the reference raster and downsampled it. We then removed its pixel values to create an empty grid of 90 meters resolution for the region and masked the non-rangeland parts of the region using NLCD 2019. We then down-

loaded the time series of Landsat and the PRISM data from September 1st, 2015 to September 1st, 2020, and preprocessed them. We retrieved the soil texture of each pixel from SoilGrids 250m dataset (Hengl et al., 2017) (Figure 4b). The majority of the region is characterized by Loam and Sandy Loam soil types. The slope and slope shape of the pixels were also extracted from the Digital Elevation Model (DEM) of the HydroSHEDS, 3 Arc-Seconds database (Lehner et al., 2008) (Figure 4c and d). We calculated the slope percentage and the profile curvature from the DEM using the "Slope" and "Curvature" tools of ESRI ArcGIS Pro 3.0.3 software, respectively. The slope shape categories were captured by the discretization of the profile curvature values such that the negative values are in the convex, the positive values are in the concave and the zero values are in the uniform shapes. Finally, the closest CLIGEN station to each pixel was obtained to get the climatic input variables of the RHEM. The region is covered by five CLIGEN stations (ne250365, ne250865, ne254455, ne256200, ne256385), with an average rainfall volume close to 7.1 mm, an average rainfall duration close to 2.4 hours, an average rainfall peak intensity close to 0.2 and, an average of 19,252 storm events in 300 years of the daily data.

3. Results and Discussion

3.1. Training loss

We split the dataset into training (90%) and validation (10%) sets to demonstrate and evaluate the loss curves of the model training. In panel (a) of Figure 5, we show the training loss curves of the model outputs. As the losses have various ranges, we divided the square roots of the losses (RMSE) by the average of the observed values for each category. All curves have similar patterns of sudden decreases at some epochs due to the learning rate decay. The two extreme curves are the Litter cover fraction (lowest) and the Biological Crusts cover fraction (highest). It means that relative to the other outputs, the model has an easier time learning the features of the Litter while cannot gain many indicative features of the Biological Crusts. It might be interpreted as less information in the input data for learning Biological Crusts compared with the rest of the outputs. Another possible reason would be the fact that the observed Biological Crusts fractions are imbalanced (only 25% of the data have non-zero Biological Crusts fractions). Even though we split the non-zero Biological Crusts among the mini-batches during the training, this problem may still be effective. The lowest graph of the foliar

cover categories is the Bunch Grass, but the Shrubs curve is not very far from it. The highest foliar cover graph is the Sod Grass fractions and it is also imbalanced (39% of the data have non-zero Sod Grass fractions). On the panel (b) We drew each curve of the panel (a) along with its corresponding validation curve (dash-dot line) in a separate plot. First, in all cases, the validation curves are stabilized after some epochs while the training curves decrease continuously. It means the model stopped learning after some time, but it is not overfitting. Second, for the Biological Crusts and Basal plots, the training curves are always higher and finish close to the validation curve. It means that in the earlier epochs, the model estimates the covers of the validation set relatively easily compared to the training set, and gradually this pattern diminished.

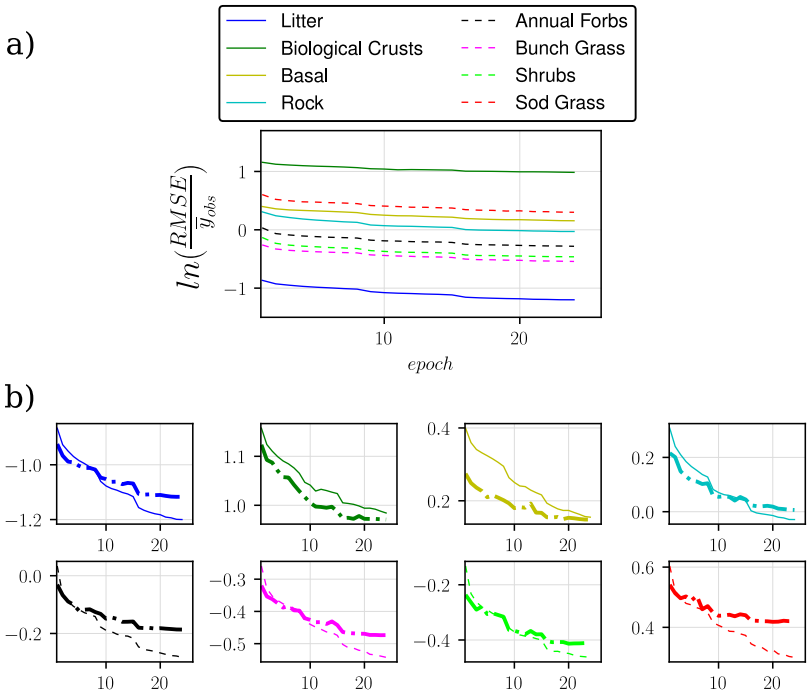

Figure 5: a) The training loss curves of the 8 model outputs. We divided the square root of the loss values (root mean squared error(RMSE)) by the average of the observed values to remove the effect of different output ranges. We also used the natural logarithms (l_n) to demonstrate the changes and differences better. b) Comparing each training loss curve of the panel (a) with its corresponding validation loss curve demonstrated with a dash-dot symbol.

3.2. The accuracy of the foliar/ground cover predictions

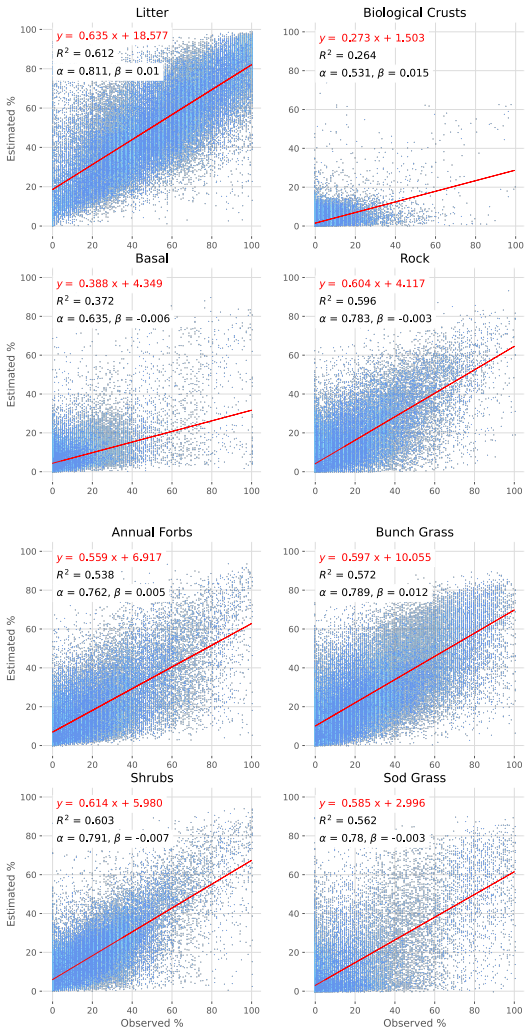

Figure 6: The model estimations versus the observed foliar/ground fractional covers from the 10-fold cross-validation for all NRI/BLM AIM plots. The equations in red show the details of the fitted lines and the R^2, α and β values in black are the measures described in section 2.3.1.

Figure 6 shows the scatter plots of the model estimations versus the observed surveyed fractional covers (in percentage) for the merged test dataset (10-fold cross-validation) along with the best-fit lines. The slopes of the fitted lines are statistically significant (p-value ≈ 0) in all cases. The strongest

Table 3: The accuracy measures of the model trained with different data sources.

Trained with NRI/Tested with BLM

	Annual Forbs	Bunch Grass	Shrubs	Sod Grass
R^2	0.498	0.374	0.473	0.297
α	0.703	0.634	0.696	0.618
β	0.019	-0.051	-0.129	0.188

	Litter	Biological Crusts*	Basal	Rock
R^2	0.461	-	-0.177	0.285
α	0.696	-	0.853	0.584
β	-0.023	-	0.474	-0.227

Trained with BLM/Tested with NRI

	Annual Forbs	Bunch Grass	Shrubs	Sod Grass
R^2	0.203	0.087	0.015	-0.153
α	0.698	0.601	1.008	0.914
β	-0.143	-0.235	0.24	0.224

	Litter	Biological Crusts*	Basal	Rock
R^2	0.194	-	-0.131	0.343
α	0.726	-	0.517	0.831
β	0.219	-	-0.201	0.154

*We did not report the measures of Biological Crusts cover because, in the NRI dataset, this fraction is extremely rare. Thus, neither training on that nor testing with it is rational.

relationship between the estimated and observed numbers is for the Litter and closely Shrubs as they have the highest slopes and R^2s while the weakest relationship is for Biological Crusts. Most of the categories have an α close to 0.8 except for the Biological Crusts and Basal covers. This means that in most cases, the variability of the model predictions is similar to the observed values. In all cases, the β measures are close to zero, indicating no significant bias in the model estimations.

Table 3 includes the details of training the model with different sources of data and comparing their accuracy. According to the results, in all cases (except for the Rock cover), estimating the BLM covers with the model trained on the NRI data produces more accurate results than the inverse experiment. One possible reason for that would be the difference between the distributions of the foliar and ground covers in the NRI and BLM datasets (Figure 3). The BLM prediction accuracy is higher for categories with sufficient data in the NRI data range. For instance, the reason for the lower accuracy in predicting Rock cover in the NRI dataset could be due to its narrower distribution compared to the BLM dataset for this category. A similar situation is observed for the Sod Grass prediction in the BLM dataset. The Litter cover category

shows a similar range in both datasets. But, the maximum of the NRI distribution aligns with the minimum of the BLM distribution. This can lead to the lower prediction accuracy of the model trained with the BLM dataset. Geography and/or land ownership may be important in predicting foliar and ground cover patterns. For instance, comparing the rangeland ownership map in the US. (Figure 2 of Robinson et al. (2019)) with the Shrubs percent map of the western US. (Figure 3 of Jones et al. (2018)) reveals that public lands contain more shrubs. The difference in shrub cover with ownership may be in part associated with respective geographic footprints.

Table 4 shows a list of previous studies of using remote sensing data to estimate the rangeland fractional covers. We only included the covers that are related to the RHEM input variables. As it was mentioned in section 1, two studies estimated the exact categories required by the RHEM and none of them are on a nationwide scale: 1- Kautz et al. (2019) only estimated the total foliar cover from Landsat data and then by two linear regressions fitted to the transect-based field-collected data they estimated the Litter and Basal covers. Our model got slightly lower R^2 and greater RMSE and MAE for the foliar cover. 2- McGwire et al. (2020) followed the same strategy and our model outperformed theirs based on the R^2 values.

The only similar nationwide study is Allred et al. (2021) which also used an ANN with multitask learning approach. Our model performed better in terms of R^2 but not RMSE and MAE for Litter and Shrubs. Considering the Annual Forbs&Grass category of their model as a combination of the Annual Forbs and Bunch/Sod Grass covers of our model, the accuracy values are comparable.

For the rest of the literature, considering the Shrubs, the R^2, RMSE, and MAE are in the ranges of (0.04,0.89), (4.18,21), and (5.6,15.3) respectively, and our results are in the middle of these ranges; for the Litter, the R^2 and RMSE are in the ranges of (0.089,0.75) and (6,11.5) respectively and our result is close to the upper limit concerning R^2 and is far higher than the RMSE range; finally, for the Forbs/Grass covers, the average R^2, RMSE, MAE values are 0.56, 13, 8.46 and our model created analogous results of 0.56, 9.32, and 7.75.

Compared to the studies that used both NRI and BLM AIM datasets, our model achieved similar accuracy for the Shrubs and Forbs/Grass covers estimation.

While comparing the accuracy measures of different studies gives us a sense of their pros and cons, there are some issues that may influence our

Table 4: A list of the previous studies on the fractional cover estimation of the US. rangelands. We only included the covers that are related to the RHEM input variables.

	Study Area	**RS Data**	**Field Data**	**Method**
Xian et al. (2013)	Arizona/New Mexico/Texas	Landsat 5/WorldView-2	collected	RT
	Litter [N/S]	Shrubs [N/S]		
R^2	0.089-0.234	0.126-0.688		
RMSE	9.4-11.5	10.4-15.8		
MAE	-	-		
Xian et al. (2015)	Nevada/California/Oregon/Idaho	Landsat 8/WorldView-2	collected	RT
	Litter [N/S]	Shrubs [N/S]		
R^2	0.19	0.34		
RMSE	6.73	8.93		
MAE	-	-		
McCord et al. (2017)	Nevada/California	Landsat 8/RapidEye	BLM(AIM)	BART
	Shrubs [A/H]			
R^2	0.37-0.55			
RMSE	5-11			
MAE	-			
Jones et al. (2018)	western U.S.	Landsat 5-8/GRIDMET	BLM/NRI	RF
	Shrubs [F/H]	Annual Forbs/grasses [F/H]		
R^2	0.04-0.43	0.19-0.49		
RMSE	7.1-10.6	10-14.8		
MAE	5.6-9.2	7.3-8.2		
Kautz et al. (2019)	Arizona	Landsat 5-8	collected	LR
	Total Foliar [F/H]	Litter (LR by field data) [A/H]	Basal (LR by field data) (B/H)	
R^2	0.85	0.29	0.57	
RMSE	5.37	28.61	4.44	
MAE	4.6	28.07	3.65	
Zhang et al. (2019)	western U.S.	Landsat 8/MODIS/ DAYMET/GDEM/STATSGO	BLM	RF
	Shrubs [F/H]	Perennial Grass [F/H]	Annual Grass [F/H]	
R^2	0.25-0.89	0.46-0.92	0.37-0.9	
RMSE	4.18-10.66	5.29-13.38	4.46-11.23	
MAE	-	-	-	
Cooper et al. (2020)	California	Landsat 8/AVIRIS	collected	RBU
	Shrubs [F/I]			
R^2	0.72			
RMSE	21			
MAE	15.3			
McGwire et al. (2020)	Utah/Colorado/New Mexico/Arizona	Landsat 8/LANDFIRE	NRI	LR
	Total Foliar [N/S]	Litter (LR by field data) [N/S]	Basal (LR by field data) [N/S]	
R^2	0.696	0.502	0.033	
RMSE	-	-	-	
MAE	-	-	-	
	Shrubs/Annual Forbs/ Bunch Grass (from LANDFIRE)			
R^2	-			
RMSE	-			
MAE	-			
Rigge et al. (2020)	western U.S.	Landsat 8/WorldView 2-3/ QuickBird/Pleiades-1/MODIS	collected	RT
	Shrubs [F/I]	Litter [F/I]		
R^2	0.37-0.73	0.35-0.75		
RMSE	6-10.6	3.8-8.9		
MAE	-	-		
Zhou et al. (2020)	western U.S.	Landsat 8/MODIS/Daymet	BLM	CNB/CART/ RF/ANN/SVR
	Total Foliar [F/H]			
R^2	0.63-0.69			
RMSE	12.33-13.47			
MAE	-			
Allred et al. (2021)	U.S. nationwide	Landsat 5-8	NRI/BLM	ANN
	Litter [F/H]	Shrubs [F/H]	Annual Forbs&Grass [F/H]	
R^2	0.31-0.37	0.08-0.57	0.19-0.58	
RMSE	7.9-11.2	7.6-12.1	7.8-13.3	
MAE	5.7-4.74	5.8-9.8	4.2-9	
Okujeni et al. (2021)	California	Landsat 7-8/AVIRIS	collected	RBU
	Shrubs [F/I]			
R^2	-			
RMSE	13.1-20.3			
MAE	9.9-14.9			

- RT: Regression Tree, BART: Bayesian additive regression trees, RF: Random Forests, LR: Linear Regression, RBU: Regression-based Unmixing, CNB: Continuous Naïve Bayes, CART: Classification and Regression Tree, SVR: Support Vector Regression.
- When a range of values is reported, the model was tested on different sets of data or by cross-validation.
- The "LR by field data" means that the reported accuracy values are from the fitted line between two field observation values. These values cannot be compared with the other numbers captured from RS estimation vs. field observation including our study.
- Method for fractional cover estimation: [F/H] First Hit, [A/H] Any Hit, [B/H] Basal Hit (Karl et al., 2017; McCord et al., 2022), [F/I]: From Vertical Image, [N/S] Not Specified

Table 5: The accuracy measures of the model to compare with the previous studies.

	Annual Forbs	Bunch Grass	Shrubs	Sod Grass	Total Foliar
R^2	0.54	0.57	0.60	0.56	0.80
RMSE(nRMSE)	12.43(0.8)	15.27(0.63)	10.5(0.66)	11.01(1.5)	11.54(0.18)
MAE(nMAE)	8.59(0.56)	11.08(0.46)	7.34(0.46)	5.7(0.78)	8.69(0.14)
	Litter	Biological Crusts	Basal	Rock	Total Ground
R^2	0.61	0.26	0.37	0.60	0.57
RMSE(nRMSE)	16.68(0.33)	5.29(2.72)	8.89(1.23)	10.69(1.01)	15.92(0.23)
MAE(nMAE)	12.58(0.25)	2.29(1.18)	5.34(0.74)	6.55(0.62)	11.67(0.17)

judgments: first, their regions of study are not the same, and different environmental factors may significantly affect the patterns of the covers; second, their dataset sizes, statistical properties, and distributions are not the same either.

Another important note here is that the exact output values of different models may not be comparable due to the differences in their fractional cover categorizations and the way that they estimated the fractional cover percentage. For instance, the rangeland cover classes (the model outputs) in Allred et al. (2021) are Annual Forbs and grasses, perennial Forbs and grasses, Shrubs, trees, Litter, and bare ground which are different from the foliar/ground cover classes of the RHEM. Also, we used the Surface Litter indicator to estimate the Litter cover (see section 1) while Allred et al. (2021) utilized the first hit (see table 4). Figure 7 compares the fractional covers estimated by the Allred et al. (2021)'s model (the average of the pixels within each NRI/BLM plot is calculated using the Rangeland Analysis Platform (`rangelands.app`)) and the observed values of the foliar/ground cover variables of the RHEM for the Shrubs and Litter covers. We chose the Shrubs and Litter since they are in both categorization systems with the same titles. However, Figure 7 shows a systematic difference between the two strategies used to define these categories, especially in the case of Litter cover. Thus, having the same class title does not mean that we can compare the outputs.

Based on the aforementioned issues, there is a need to establish a standard model accuracy report system so the studies on rangeland cover estimation could be adaptable and fully comparable.

3.3. The RHEM outputs by the observed covers versus the predicted covers

Figure 8 depicts the scatter plots of the RHEM outputs using the observed covers versus the predicted covers. Part (a) is for all the field data plots (both

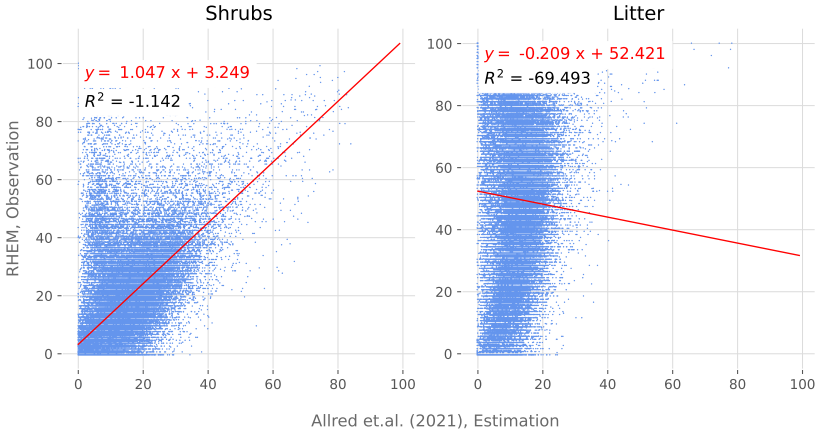

Figure 7: The Shrubs and Litter fractional covers estimated by the Allred et al. (2021) model versus the observed values of the foliar/ground cover variables of the RHEM. Note that the Litter cover in Allred et al. (2021) is estimated by the first hit indicator while our Litter estimation for the RHEM is by the Surface Litter indicator (see section 1 for more details).

the NRI and BLM data) while part (b) is for the NRI data and part (c) is for the BLM data. The R^2 value for the runoff is close to 0.9 in all parts while for the soil loss and sediment yield is close to 0.4 in parts (a) and (b) and 0.5 in part (c). The α value for the runoff is close to 0.95 for the runoff in all parts while it is close to 0.5 in parts (a) and (b) and is close to 0.65 in part (c) for the soil loss and sediment yield. The β value for the runoff is close to -0.01 in all parts while it is -0.06, -0.07, and, -0.04 in parts (a), (b), and, (c) respectively for the soil loss and sediment yield. The slope of the fitted line for the runoff in all cases is close to 0.9 while this value for the runoff and sediment yield is close to 0.3 in parts (a) and (b) and close to 0.45 in part (c). These measures show that the estimated runoff using the predicted covers has 1- A stronger relationship with the observed values, 2- A closer variability to the observed values, and 3- A lower estimation bias than the estimated soil loss and sediment yield. The higher accuracy of the runoff is because of its lower sensitivity to the foliar and ground covers compared with the soil loss and sediment yield (Saeedimoghaddam et al., 2022). Also, the accuracy of the estimated RHEM outputs for the BLM data is higher than the NRI data, especially for soil loss and sediment yield. This is because the foliar/ground cover estimator is more accurate in BLM public lands (see section 3.2).

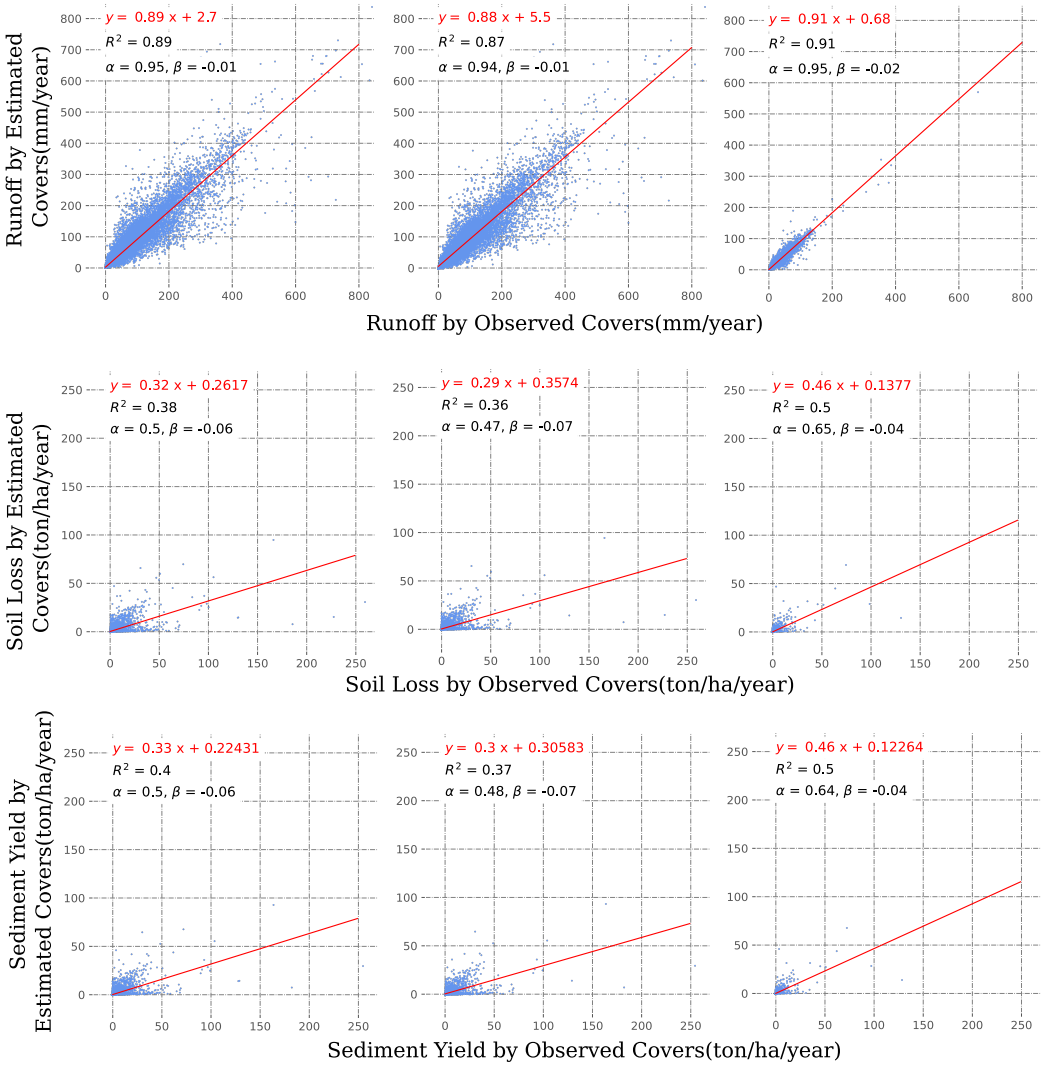

Figure 8: The RHEM outputs using the observed covers versus the predicted covers for left: all field data plots, middle: NRI field data plots, and, right: BLM field data plots.

3.4. Mapping the RHEM outputs

Figure 9 exhibits the maps of the RHEM outputs for Summer, 2020. The runoff is mostly between 10 and 50 mm/year, the soil loss is mostly less than 0.5 ton/ha/year and, the sediment yield is mostly less than 0.2 ton/ha/year. The runoff is significantly sensitive to soil texture and climatic variables (Saeedimoghaddam et al., 2022). The effect of the soil texture

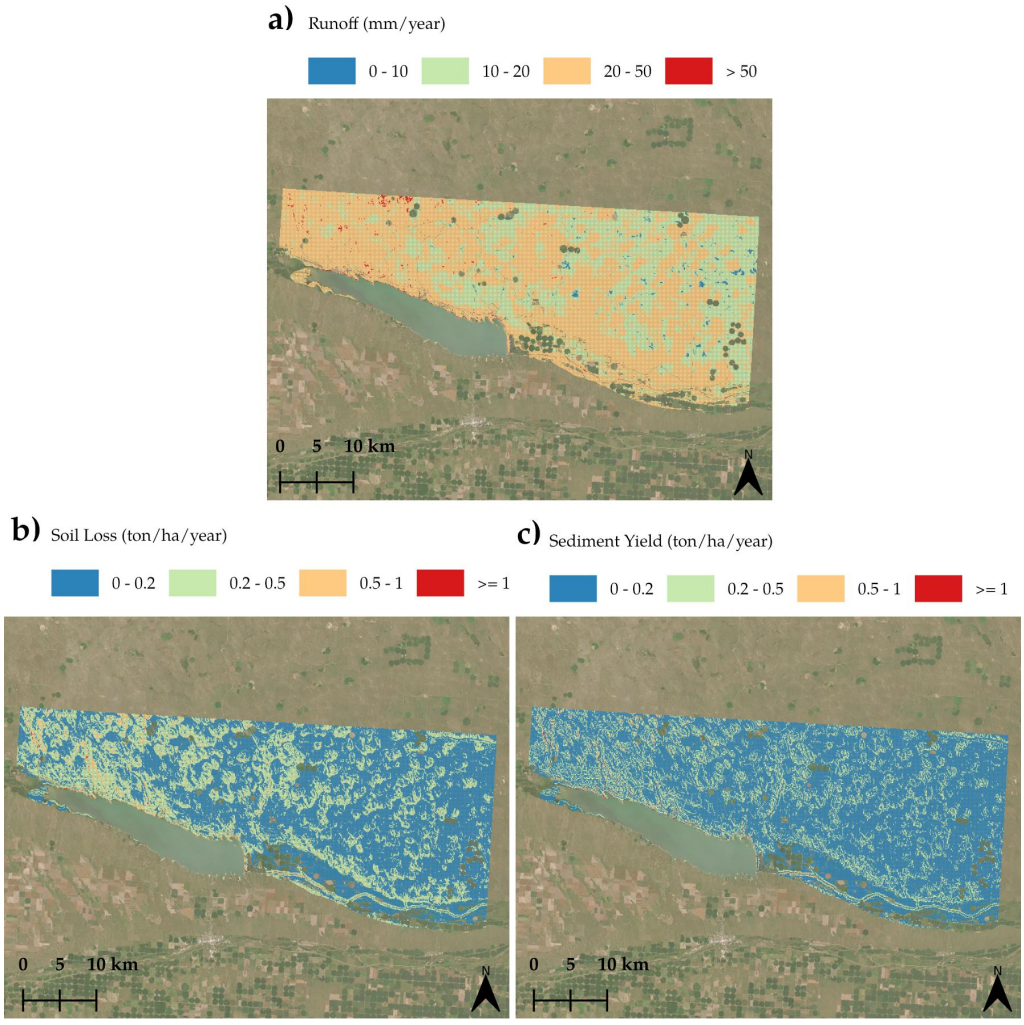

Figure 9: The map of a) average annual runoff (mm/year), b) average annual soil loss (ton/ha/year), and, c) average annual sediment yield (ton/ha/year)

variable can be visually recognized by comparing the runoff map and the soil texture map in Figure 4b (The visual inspection of the climatic maps does not reveal their effects because the process of assigning the closest station to each pixel creates the maps with sharp and synthetic borders). On the other hand, slope and total ground cover have the most effects on soil loss and sediment yield. Also, the slope shape is more effective on the sediment yield than the soil loss (Saeedimoghaddam et al., 2022). Visually comparing

Figure 4c and 4d with the soil loss and the sediment yield maps reveals the slope and slope shape effects. Figure 10 shows the map of the total ground cover of the region. The western part of the region has less ground cover than the eastern part and, as expected, the western part has greater soil loss than the western part. However, for the sediment yield, such a spatial relationship cannot be revealed by a visual inspection.

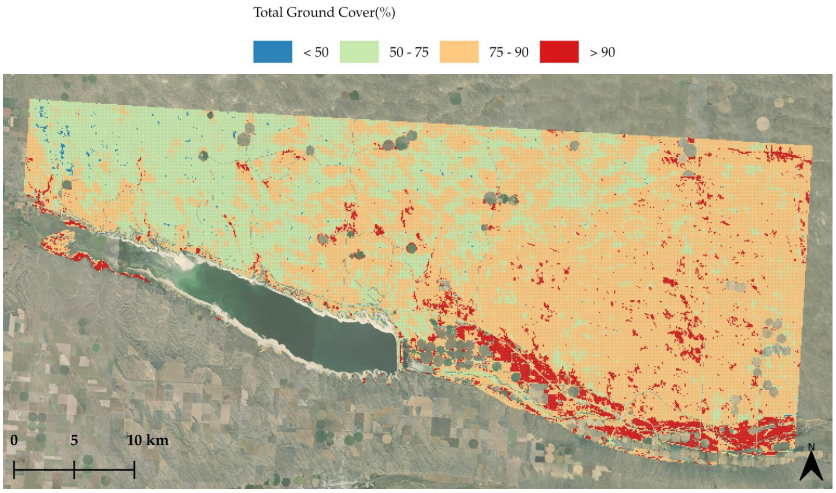

Figure 10: The total ground cover map of the region

4. Conclusion

In this study, we developed an ANN that estimates the foliar/ground cover input variables of the RHEM for any point of interest in the rangelands of the US in any season of any year after 1987. The ANN model uses RS data, soil type data, and the latitude and longitude of the point. We trained the ANN on three different field data sources. Using the estimated covers, we were able to reproduce the actual RHEM outputs with $R^2 \approx 90\%$ for the runoff and $R^2 \approx 40\%$ for the soil loss and sediment yield. The ANN enabled us to estimate the covers for a region of interest and create RHEM maps. Creating such maps is crucial for rangeland management because (i) it helps the land managers to allocate resources and make informed decisions according to the past and the current conditions of a region and (ii) it allows them to assess the outcome of their decisions on a continuous map on different dates.

In addition to the slope information, the soil loss and the sediment yield are mostly controlled by the ground cover variables. Thus, improving the accuracy of the model prediction for those variables could increase the precision of the soil loss and the sediment yield. The ANN model is less accurate for Biological Crusts and Basal covers. We expected difficulty in estimating the Basal cover using downward-looking RS data (Kautz et al., 2019). However, the underestimation of the Biological Crusts is an effect of imbalanced data in this category (see section 3.1). One way to improve the accuracy of the Biological Crusts estimation is by adding new observations with the non-zero Biological Crusts category to the dataset. Since surveying would require substantial resources, alternative strategies such as data augmentation by Generative Adversarial Networks (GAN) could be helpful in addressing the imbalanced data problem (Mariani et al., 2018; Quintana et al., 2020; Al-Najjar et al., 2021).

The Litter cover is also an important category among the ground covers. In more than 80% of the cases in our dataset, the Litter cover is the dominant category with a relatively large value. As a result, improving the Litter estimation of the ANN could dramatically improve the RHEM estimation. Among the bands of the RS data, SWIR is the most useful one in capturing the plant Litter information (Jacques et al., 2014; Li and Guo, 2018). Adding an input channel to the ANN model, which includes the RS data with more SWIR bands, could improve the Litter cover estimation.

Data Availability Statement

The preprocessed remote sensing data along with the RHEM outputs of the field data plots, our training pipeline, all of the Python scripts we used for cross-validation, and our model's pre-trained weights are open source and publicly available via `https://github.com/saeedimd/RHEM-ML.git`. Due to data restrictions on the NRI dataset, we removed the latitude and longitude details of the field data plots from the repository.

Acknowledgement

This material is based upon work supported by the U.S. Department of Agriculture, Natural Resources Conservation Service, Conservation Effects Assessment Project (CEAP) Grazing Lands Component, under agreement number NR193A750007C002.

References

Abadi, M., Agarwal, A., Barham, P., Brevdo, E., Chen, Z., Citro, C., Corrado, G.S., Davis, A., Dean, J., Devin, M., Ghemawat, S., Goodfellow, I., Harp, A., Irving, G., Isard, M., Jia, Y., Jozefowicz, R., Kaiser, L., Kudlur, M., Levenberg, J., Mané, D., Monga, R., Moore, S., Murray, D., Olah, C., Schuster, M., Shlens, J., Steiner, B., Sutskever, I., Talwar, K., Tucker, P., Vanhoucke, V., Vasudevan, V., Viégas, F., Vinyals, O., Warden, P., Wattenberg, M., Wicke, M., Yu, Y., Zheng, X., 2015. TensorFlow: Large-scale machine learning on heterogeneous systems. URL: `www.tensorflow.org/`. software available from tensorflow.org.

Abdolalizadeh, Z., Ghorbani, A., Mostafazadeh, R., Moameri, M., 2020. Rangeland canopy cover estimation using landsat oli data and vegetation indices in sabalan rangelands, iran. Arabian Journal of Geosciences 13, 245. doi:`10.1007/s12517-020-5150-1`.

Airbus, 2022. Copernicus DEM: Copernicus digital elevation model product handbook. European Space Agency. URL: `https://spacedata.copernicus.eu/documents/20123/121239/GEO1988-CopernicusDEM-SPE-002_ProductHandbook_I4.0.pdf`.

Al-Hamdan, O.Z., Hernandez, M., Pierson, F.B., Nearing, M.A., Williams, C.J., Stone, J.J., Boll, J., Weltz, M.A., 2015. Rangeland hydrology and erosion model (rhem) enhancements for applications on disturbed rangelands. Hydrological Processes 29, 445–457. doi:`10.1002/hyp.10167`.

Al-Najjar, H.A.H., Pradhan, B., Sarkar, R., Beydoun, G., Alamri, A., 2021. A new integrated approach for landslide data balancing and spatial prediction based on generative adversarial networks (gan). Remote Sensing 13. doi:`10.3390/rs13194011`.

Allred, B.W., Bestelmeyer, B.T., Boyd, C.S., Brown, C., Davies, K.W., Duniway, M.C., Ellsworth, L.M., Erickson, T.A., Fuhlendorf, S.D., Griffiths, T.V., Jansen, V., Jones, M.O., Karl, J., Knight, A., Maestas, J.D., Maynard, J.J., McCord, S.E., Naugle, D.E., Starns, H.D., Twidwell, D., Uden, D.R., 2021. Improving landsat predictions of rangeland fractional cover with multitask learning and uncertainty. Methods in Ecology and Evolution 12, 841–849. doi:`10.1111/2041-210X.13564`.

Bedunah, D.J., Angerer, J.P., 2012. Rangeland degradation, poverty, and conflict: How can rangeland scientists contribute to effective responses and solutions? Rangeland Ecology & Management 65, 606–612. doi:10.2111/REM-D-11-00155.1.

Cao, X., Chen, J., Matsushita, B., Imura, H., 2010. Developing a modis-based index to discriminate dead fuel from photosynthetic vegetation and soil background in the asian steppe area. International Journal of Remote Sensing 31, 1589–1604. doi:10.1080/01431160903475274.

Chen, Y., Gillieson, D., 2009. Evaluation of landsat tm vegetation indices for estimating vegetation cover on semi-arid rangelands: a case study from australia. Canadian Journal of Remote Sensing 35, 435–446. doi:10.5589/m09-037.

Cooper, S., Okujeni, A., Jänicke, C., Clark, M., van der Linden, S., Hostert, P., 2020. Disentangling fractional vegetation cover: Regression-based unmixing of simulated spaceborne imaging spectroscopy data. Remote Sensing of Environment 246, 111856. doi:10.1016/j.rse.2020.111856.

Crist, E.P., 1985. A tm tasseled cap equivalent transformation for reflectance factor data. Remote Sensing of Environment 17, 301–306. doi:10.1016/0034-4257(85)90102-6.

Flanagan, D.C., Ascough, J.C., Nearing, M.A., Laflen, J.M., 2001. The Water Erosion Prediction Project (WEPP) Model. Springer US, Boston, MA. chapter 7. pp. 145–199. doi:10.1007/978-1-4615-0575-4_7.

Gedefaw, M.G., Geli, H.M.E., Abera, T.A., 2021. Assessment of rangeland degradation in new mexico using time series segmentation and residual trend analysis (tss-restrend). Remote Sensing 13. doi:10.3390/rs13091618.

Geerken, R., Ilaiwi, M., 2004. Assessment of rangeland degradation and development of a strategy for rehabilitation. Remote Sensing of Environment 90, 490–504. doi:10.1016/j.rse.2004.01.015.

Gorelick, N., Hancher, M., Dixon, M., Ilyushchenko, S., Thau, D., Moore, R., 2017. Google earth engine: Planetary-scale geospatial analysis for everyone. Remote Sensing of Environment doi:10.1016/j.rse.2017.06.031.

Gupta, H.V., Kling, H., Yilmaz, K.K., Martinez, G.F., 2009. Decomposition of the mean squared error and nse performance criteria: Implications for improving hydrological modelling. Journal of Hydrology 377, 80–91. doi:10.1016/j.jhydrol.2009.08.003.

Gupta, H.V., Sorooshian, S., Yapo, P.O., 1999. Status of automatic calibration for hydrologic models: Comparison with multilevel expert calibration. Journal of Hydrologic Engineering 4, 135–143. URL: https://ascelibrary.org/doi/abs/10.1061/%28ASCE%291084-0699%281999%294%3A2%28135%29, doi:10.1061/(ASCE)1084-0699(1999)4:2(135).

He, K., Zhang, X., Ren, S., Sun, J., 2015. Delving deep into rectifiers: Surpassing human-level performance on imagenet classification, in: 2015 IEEE International Conference on Computer Vision (ICCV), IEEE Computer Society, Los Alamitos, CA, USA. pp. 1026–1034. doi:10.1109/ICCV.2015.123.

Hengl, T., Mendes de Jesus, J., Heuvelink, G.B.M., Ruiperez Gonzalez, M., Kilibarda, M., Blagotić, A., Shangguan, W., Wright, M.N., Geng, X., Bauer-Marschallinger, B., Guevara, M.A., Vargas, R., MacMillan, R.A., Batjes, N.H., Leenaars, J.G.B., Ribeiro, E., Wheeler, I., Mantel, S., Kempen, B., 2017. Soilgrids250m: Global gridded soil information based on machine learning. PLOS ONE 12, 1–40. doi:10.1371/journal.pone.0169748.

Hernandez, M., Nearing, M., Stone, J., Pierson, F., Wei, H., Spaeth, K., Heilman, P., Weltz, M., Goodrich, D., 2013. Application of a rangeland soil erosion model using national resources inventory data in southeastern arizona. Journal of Soil and Water Conservation 68, 512–525. doi:10.2489/jswc.68.6.512.

Hernandez, M., Nearing, M.A., Al-Hamdan, O.Z., Pierson, F.B., Armendariz, G., Weltz, M.A., Spaeth, K.E., Williams, C.J., Nouwakpo, S.K., Goodrich, D.C., Unkrich, C.L., Nichols, M.H., Holifield Collins, C.D., 2017. The rangeland hydrology and erosion model: A dynamic approach for predicting soil loss on rangelands. Water Resources Research 53, 9368–9391. doi:10.1002/2017WR020651.

Herrick, J., Van Zee, J., McCord, S., Courtright, E., Karl, J., Burkett, L., 2018. Monitoring manual for grassland, shrubland, and savanna ecosystems, Volume 1: core methods. USDA-ARS Jornada Experimental Range Las Cruces, New Mexico. URL: www.blm.gov/sites/blm.gov/files/docs/2022-04/TR_1734_8_vol1_508.pdf.

Jacques, D.C., Kergoat, L., Hiernaux, P., Mougin, E., Defourny, P., 2014. Monitoring dry vegetation masses in semi-arid areas with modis swir bands. Remote Sensing of Environment 153, 40–49. doi:https://doi.org/10.1016/j.rse.2014.07.027.

Jansen, V.S., Kolden, C.A., Schmalz, H.J., 2018. The development of near real-time biomass and cover estimates for adaptive rangeland management using landsat 7 and landsat 8 surface reflectance products. Remote Sensing 10. doi:10.3390/rs10071057.

Jansen, V.S., Kolden, C.A., Taylor, R.V., Newingham, B.A., 2016. Quantifying livestock effects on bunchgrass vegetation with landsat etm+ data across a single growing season. International Journal of Remote Sensing 37, 150–175. doi:10.1080/01431161.2015.1117681.

Jones, M.O., Allred, B.W., Naugle, D.E., Maestas, J.D., Donnelly, P., Metz, L.J., Karl, J., Smith, R., Bestelmeyer, B., Boyd, C., Kerby, J.D., McIver, J.D., 2018. Innovation in rangeland monitoring: annual, 30 m, plant functional type percent cover maps for u.s. rangelands, 1984–2017. Ecosphere 9, e02430. doi:10.1002/ecs2.2430.

Kachergis, E., Miller, S.W., McCord, S.E., Dickard, M., Savage, S., Reynolds, L.V., Lepak, N., Dietrich, C., Green, A., Nafus, A., Prentice, K., Davidson, Z., 2022. Adaptive monitoring for multiscale land management: Lessons learned from the assessment, inventory, and monitoring (aim) principles. Rangelands 44, 50–63. doi:https://doi.org/10.1016/j.rala.2021.08.006. adaptive Monitoring to Support Adaptive Management.

Karl, J.W., McCord, S.E., Hadley, B.C., 2017. A comparison of cover calculation techniques for relating point-intercept vegetation sampling to remote sensing imagery. Ecological Indicators 73, 156–165. URL: https://www.sciencedirect.com/science/article/pii/S1470160X16305659, doi:https://doi.org/10.1016/j.ecolind.2016.09.034.

Karnieli, A., 1997. Development and implementation of spectral crust index over dune sands. International Journal of Remote Sensing 18, 1207–1220. doi:10.1080/014311697218368.

Kautz, M.A., Holifield Collins, C.D., Guertin, D.P., Goodrich, D.C., van Leeuwen, W.J., Williams, C.J., 2019. Hydrologic model parameterization using dynamic landsat-based vegetative estimates within a semiarid grassland. Journal of Hydrology 575, 1073–1086. doi:10.1016/j.jhydrol.2019.05.044.

Kingma, D.P., Ba, J., 2014. Adam: A Method for Stochastic Optimization. doi:10.48550/arXiv.1412.6980.

Lehner, B., Verdin, K., Jarvis, A., 2008. New global hydrography derived from spaceborne elevation data. Eos, Transactions American Geophysical Union 89, 93–94. doi:https://doi.org/10.1029/2008EO100001.

Li, Z., Guo, X., 2018. Non-photosynthetic vegetation biomass estimation in semiarid canadian mixed grasslands using ground hyperspectral data, landsat 8 oli, and sentinel-2 images. International Journal of Remote Sensing 39, 6893–6913. doi:10.1080/01431161.2018.1468105.

Liu, G., Reda, F.A., Shih, K.J., Wang, T.C., Tao, A., Catanzaro, B., 2018. Image inpainting for irregular holes using partial convolutions, in: Ferrari, V., Hebert, M., Sminchisescu, C., Weiss, Y. (Eds.), Computer Vision – ECCV 2018, Springer International Publishing, Cham. pp. 89–105. doi:10.1007/978-3-030-01252-6_6.

Mariani, G., Scheidegger, F., Istrate, R., Bekas, C., Malossi, C., 2018. Bagan: Data augmentation with balancing gan. doi:10.48550/ARXIV.1803.09655.

McCord, S.E., Brehm, J.R., Burnett, S.H., Dietrich, C., Edwards, B., Metz, L.J., Hernandez Narvaez and Fred Pierson and Kelly S. Ramirez and Nelson G. Stauffer and Nicholas P. Webb and Craig E. Tweedie, M., 2022. A framework and toolset for standardizing agroecosystem indicators. Ecological Indicators 144, 109511. doi:https://doi.org/10.1016/j.ecolind.2022.109511.

McCord, S.E., Buenemann, M., Karl, J.W., Browning, D.M., Hadley, B.C., 2017. Integrating remotely sensed imagery and existing multiscale

field data to derive rangeland indicators: Application of bayesian additive regression trees. Rangeland Ecology & Management 70, 644–655. doi:10.1016/j.rama.2017.02.004.

McGwire, K.C., Weltz, M.A., Nouwakpo, S., Spaeth, K., Founds, M., Cadaret, E., 2020. Mapping erosion risk for saline rangelands of the mancos shale using the rangeland hydrology erosion model. Land Degradation & Development 31, 2552–2564. doi:10.1002/ldr.3620.

N. Moriasi, D., G. Arnold, J., W. Van Liew, M., L. Bingner, R., D. Harmel, R., L. Veith, T., 2007. Model evaluation guidelines for systematic quantification of accuracy in watershed simulations. Transactions of the ASABE 50, 885–900. URL: https://elibrary.asabe.org/abstract.asp?aid=23153&t=3.

Naji, T.A.H., 2018. Study of vegetation cover distribution using DVI, PVI, WDVI indices with 2d-space plot. Journal of Physics: Conference Series 1003, 012083. doi:10.1088/1742-6596/1003/1/012083.

Nauman, T.W., Ely, C.P., Miller, M.P., Duniway, M.C., 2019. Salinity yield modeling of the upper colorado river basin using 30-m resolution soil maps and random forests. Water Resources Research 55, 4954–4973. doi:10.1029/2018WR024054.

Nearing, M.A., Wei, H., J. Stone, J., B. Pierson, F., E. Spaeth, K., A. Weltz, M., C. Flanagan, D., Hernandez, M., 2011. A rangeland hydrology and erosion model. Transactions of the ASABE 54, 901–908. doi:10.13031/2013.37115.

Nelson, K.J., Long, D.G., Connot, J.A., 2016. LANDFIRE 2010—Updates to the national dataset to support improved fire and natural resource management. Technical Report. U.S. Department of the Interior, U.S. Geological Survey. Reston, VA. doi:10.3133/ofr20161010. report.

Nicks, A., Lane, L., Gander, G., 1995. Weather generator, in: Flanagan, D., Nearing, M. (Eds.), USDA-water erosion prediction project Hillslope profile and watershed model documentation (Chapter 2). USDA-ARS National Soil Erosion Research Laboratory, West Lafayette, IN: USDA-ARS National Soil Erosion. URL: https://www.ars.usda.gov/ARSUserFiles/50201000/WEPP/chap2.pdf.

Nusser, S.M., Goebel, J.J., 1997. The national resources inventory: a long-term multi-resource monitoring programme. Environmental and Ecological Statistics 4, 181–204. doi:10.1023/A:1018574412308.

Okujeni, A., Jänicke, C., Cooper, S., Frantz, D., Hostert, P., Clark, M., Segl, K., van der Linden, S., 2021. Multi-season unmixing of vegetation class fractions across diverse californian ecoregions using simulated spaceborne imaging spectroscopy data. Remote Sensing of Environment 264, 112558. doi:10.1016/j.rse.2021.112558.

Oregon State University, 2014. Prism climate group. URL: https://prism.oregonstate.edu. accessed 16 Dec 2020.

Pei, J., Wang, L., Huang, N., Geng, J., Cao, J., Niu, Z., 2018. Analysis of landsat-8 oli imagery for estimating exposed bedrock fractions in typical karst regions of southwest china using a karst bare-rock index. Remote Sensing 10. doi:10.3390/rs10091321.

Pierson, F.B., Jason Williams, C., Hardegree, S.P., Weltz, M.A., Stone, J.J., Clark, P.E., 2011. Fire, plant invasions, and erosion events on western rangelands. Rangeland Ecology & Management 64, 439–449. doi:https://doi.org/10.2111/REM-D-09-00147.1.

Quintana, M., Schiavon, S., Tham, K.W., Miller, C., 2020. Balancing thermal comfort datasets: We gan, but should we?, in: Proceedings of the 7th ACM International Conference on Systems for Energy-Efficient Buildings, Cities, and Transportation, Association for Computing Machinery, New York, NY, USA. p. 120–129. doi:10.1145/3408308.3427612.

Rigge, M., Homer, C., Cleeves, L., Meyer, D.K., Bunde, B., Shi, H., Xian, G., Schell, S., Bobo, M., 2020. Quantifying western u.s. rangelands as fractional components with multi-resolution remote sensing and in situ data. Remote Sensing 12. doi:10.3390/rs12030412.

Robinson, N.P., Allred, B.W., Naugle, D.E., Jones, M.O., 2019. Patterns of rangeland productivity and land ownership: Implications for conservation and management. Ecological Applications 29, e01862. doi:10.1002/eap.1862.

Rollins, M.G., 2009. Landfire: a nationally consistent vegetation, wildland fire, and fuel assessment. International Journal of Wildland Fire 18, 235–249. doi:10.1071/WF08088.

Roy, D., Kovalskyy, V., Zhang, H., Vermote, E., Yan, L., Kumar, S., Egorov, A., 2016. Characterization of landsat-7 to landsat-8 reflective wavelength and normalized difference vegetation index continuity. Remote Sensing of Environment 185, 57–70. doi:10.1016/j.rse.2015.12.024. landsat 8 Science Results.

Saeedimoghaddam, M., Nearing, G., Hernandez, M., Nearing, M., Goodrich, D., Metz, L., 2022. An artificial neural network emulator of the rangeland hydrology and erosion model. EarthArxiv doi:10.31223/x5n93j.

Sayler, K., Zanter, K., 2020a. Landsat 4-7 collection 1 (c1) surface reflectance (ledaps) product guide. URL: www.usgs.gov/media/files/landsat-4-7-collection-1-surface-reflectance-code-ledaps-product-guide.

Sayler, K., Zanter, K., 2020b. Landsat 8 collection 1 (c1) land surface reflectance code (lasrc) product guide. URL: www.usgs.gov/media/files/landsat-8-collection-1-land-surface-reflectance-code-product-guide.

Schlesinger, W.H., Abrahams, A.D., Parsons, A.J., Wainwright, J., 1999. Nutrient losses in runoff from grassland and shrubland habitats in southern new mexico: I. rainfall simulation experiments. Biogeochemistry 45, 21–34. doi:10.1007/BF00992871.

Schlesinger, W.H., Raikes, J.A., Hartley, A.E., Cross, A.F., 1996. On the spatial pattern of soil nutrients in desert ecosystems. Ecology 77, 364–374. doi:https://doi.org/10.2307/2265615.

Senseman, G.M., Bagley, C.F., Tweddale, S.A., 1996. Correlation of rangeland cover measures to satellite-imagery-derived vegetation indices. Geocarto International 11, 29–38. doi:10.1080/10106049609354546.

Sivanpillai, R., Booth, D.T., 2008. Characterizing rangeland vegetation using landsat and 1-mm vlsa data in central wyoming (usa). Agroforestry Systems 73, 55–64. doi:10.1007/s10457-008-9115-8.

Soil Survey Staff, S.C.S., 1999. Soil taxonomy: A basic system of soil classification for making and interpreting soil surveys. Agriculture handbook 436. 2nd ed., Natural Resources Conservation Service. U.S. Department of Agriculture. URL: https://www.nrcs.usda.gov/Internet/FSE_DOCUMENTS/nrcs142p2_051232.pdf.

Srivastava, N., Hinton, G., Krizhevsky, A., Sutskever, I., Salakhutdinov, R., 2014. Dropout: A simple way to prevent neural networks from overfitting. Journal of Machine Learning Research 15, 1929–1958. URL: jmlr.org/papers/v15/srivastava14a.html.

Toevs, G.R., Karl, J.W., Taylor, J.J., Spurrier, C.S., Karl, M.S., Bobo, M.R., Herrick, J.E., 2011. Consistent indicators and methods and a scalable sample design to meet assessment, inventory, and monitoring information needs across scales. Rangelands 33, 14–20. doi:10.2111/1551-501X-33.4.14.

Turnbull, L., Wainwright, J., Brazier, R.E., 2010. Changes in hydrology and erosion over a transition from grassland to shrubland. Hydrological Processes 24, 393–414. doi:https://doi.org/10.1002/hyp.7491.

Turnbull, L., Wilcox, B.P., Belnap, J., Ravi, S., D'Odorico, P., Childers, D., Gwenzi, W., Okin, G., Wainwright, J., Caylor, K.K., Sankey, T., 2012. Understanding the role of ecohydrological feedbacks in ecosystem state change in drylands. Ecohydrology 5, 174–183. doi:https://doi.org/10.1002/eco.265.

USDA, 2020. Gridded soil survey geographic (gssurgo) database. URL: https://www.nrcs.usda.gov/wps/portal/nrcs/detail/soils/survey/geo/?cid=nrcs142p2_053628.

USDA, 2022. Land resource regions and major land resource areas of the united states, the caribbean, and the pacific basin, in: Agriculture Handbook 296. U.S. Department of Agriculture. URL: https://www.nrcs.usda.gov/sites/default/files/2022-10/AgHandbook296_text_low-res.pdf.

USDA, N.R.C.S., 2018. National resources inventory: Grazing land onsite data study, 2004-2018 data provided by usda nrcs for purposes of this

project. URL: www.nrcs.usda.gov/wps/portal/nrcs/main/national/technical/nra/nri/".

Weltz, M., Jolley, L., Hernandez, M., E. Spaeth, K., Rossi, C., Talbot, C., Nearing, M., Stone, J., Goodrich, D., Pierson, F., Wei, H., Morris, C., 2014. Estimating conservation needs for rangelands using usda national resources inventory assessments. Transactions of the ASABE 57, 1559–1570. doi:10.13031/trans.57.10030.

Wickham, J., Stehman, S.V., Sorenson, D.G., Gass, L., Dewitz, J.A., 2021. Thematic accuracy assessment of the nlcd 2016 land cover for the conterminous united states. Remote Sensing of Environment 257, 112357. doi:https://doi.org/10.1016/j.rse.2021.112357.

Williams, C.J., Pierson, F.B., Al-Hamdan, O.Z., Kormos, P.R., Hardegree, S.P., Clark, P.E., 2014. Can wildfire serve as an ecohydrologic threshold-reversal mechanism on juniper-encroached shrublands. Ecohydrology 7, 453–477. doi:https://doi.org/10.1002/eco.1364.

Williams, C.J., Pierson, F.B., Al-Hamdan, O.Z., Nouwakpo, S.K., Johnson, J.C., Polyakov, V.O., Kormos, P.R., Shaff, S.E., Spaeth, K.E., 2022. Assessing runoff and erosion on woodland-encroached sagebrush steppe using the rangeland hydrology and erosion model. Ecosphere 13, e4145. doi:https://doi.org/10.1002/ecs2.4145.

Woznicki, S.A., Cada, P., Wickham, J., Schmidt, M., Baynes, J., Mehaffey, M., Neale, A., 2020. Sediment retention by natural landscapes in the conterminous united states. Science of The Total Environment 745, 140972. doi:10.1016/j.scitotenv.2020.140972.

Xian, G., Homer, C., Meyer, D., Granneman, B., 2013. An approach for characterizing the distribution of shrubland ecosystem components as continuous fields as part of nlcd. ISPRS Journal of Photogrammetry and Remote Sensing 86, 136–149. doi:10.1016/j.isprsjprs.2013.09.009.

Xian, G., Homer, C., Rigge, M., Shi, H., Meyer, D., 2015. Characterization of shrubland ecosystem components as continuous fields in the northwest united states. Remote Sensing of Environment 168, 286–300. doi:10.1016/j.rse.2015.07.014.

Yu, C.L., Li, J., Karl, M.G., Krueger, T.J., 2020. Obtaining a balanced area sample for the bureau of land management rangeland survey. Journal of Agricultural, Biological and Environmental Statistics 25, 250–275. doi:10.1007/s13253-020-00392-5.

Zhang, J., Okin, G.S., Zhou, B., 2019. Assimilating optical satellite remote sensing images and field data to predict surface indicators in the western u.s.: Assessing error in satellite predictions based on large geographical datasets with the use of machine learning. Remote Sensing of Environment 233, 111382. doi:10.1016/j.rse.2019.111382.

Zhang, Y., Schaap, M.G., 2017. Weighted recalibration of the rosetta pedotransfer model with improved estimates of hydraulic parameter distributions and summary statistics (rosetta3). Journal of Hydrology 547, 39–53. doi:https://doi.org/10.1016/j.jhydrol.2017.01.004.

Zhou, B., Okin, G.S., Zhang, J., 2020. Leveraging google earth engine (gee) and machine learning algorithms to incorporate in situ measurement from different times for rangelands monitoring. Remote Sensing of Environment 236, 111521. doi:10.1016/j.rse.2019.111521.